

The detections of inflowing gas from narrow absorption lines at the parsec scale

Zhi-Fu Chen^{1,4,6*}, Minfeng Gu^{2*}, Zhicheng He^{3*}, Defu Bu², Fulai Guo², Qiusheng Gu⁴, and Yiping Qin⁵

¹ Department of physics, Guangxi University for Nationalities, Nanning 530006, China; zhichenfu@126.com

² Key Laboratory for Research in Galaxies and Cosmology, Shanghai Astronomical Observatory, Chinese Academy of Sciences, Shanghai 200030, China; gumf@shao.ac.cn

³ School of Astronomy and Space Science, University of Science and Technology of China, Hefei, China; zcho@ustc.edu.cn

⁴ School of Astronomy and Space Science, Nanjing University, Nanjing 210093, China

⁵ Center for Astrophysics, Guangzhou University, Guangzhou 510006, China

⁶ School of Materials Science and Engineering, Baise University, Baise 533000, China

December 15, 2021

ABSTRACT

Inflows at the dusty torus and smaller scales is crucial to investigate the process of supermassive black hole accretion. However, only few cases of inflowing gas at small scales have been reported through redshifted broad absorption lines so far. Here we report 9 redshifted narrow absorption lines (NALs) of Mg⁺ ions with inflowing speeds of 1071 — 1979 km s⁻¹, which are likely along the directions close to the axes of accretion disks. The quasars showing inflowing Mg II NALs have on average slightly smaller Eddington ratios when compared to the sources with outflow Mg II NALs. The upper limits of locations of the detected NALs are at parsec scale, around the distances of dusty tori to central SMBHs. The one possible origin of these infalling NALs is from dusty tori. Of course, these infalling NALs can also be naturally explained by chaotic cold accretion resulted from the nonlinear interaction of active galactic nucleus (AGN) jets with the interstellar medium, and these cold gaseous blobs may originally precipitate in metal-rich trailing outflows uplifted by AGN jet ejecta. The infalling NALs may thus provide direct evidence for cold gas precipitation and accretion in AGN feedback processes, and provide the direct evidence of inflowing gas along the directions close to quasar jets and at parsec scale. It does not matter whether these infalling NALs are from the dusty tori or the interaction of AGN jets with the ISM, the infalling NALs cannot provide sufficient fuels to power the quasars.

Key words. galaxy physics — galaxies: active — quasars: absorption lines — galaxies: inflall

1. Introduction

Quasars are one of the brightest astronomical objects powered by accretion disks surrounding supermassive black holes (SMBHs). Numerous evidences (e.g., Ferrarese & Merritt 2000; Gu et al. 2009; Aird et al. 2010; Madau & Dickinson 2014) have revealed that SMBHs and their host galaxies co-evolve (e.g., Kormendy & Ho 2013; Heckman & Best 2014). Feed and feedback are fundamental processes resulting in the co-evolution of SMBHs and galaxies. In the forms of jets, outflows, winds, and radiations, quasar feedback might heat and blow off the gas from central region of the host galaxy (e.g., Elvis 2000; Gaspari & Sądowski 2017). This process likely compress the star formation within host galaxy, regulate the galaxy growth to be become overmassive, and impact on the surrounding circumgalactic medium (CGM) and intergalactic medium (IGM).

The trigger of nuclear activity requires gas supply, from a fraction to dozens of solar masses per year (e.g., Storchi-Bergmann & Schnorr-Müller 2019), to feed the Active Galactic Nuclei (AGN). Although galaxy interactions and mergers can efficiently trigger and feed the quasars (e.g., Simões Lopes et al. 2007; Treister et al. 2012; Menci et al. 2014; Gatti et al. 2015; Gaspari & Sądowski

2017; Storchi-Bergmann & Schnorr-Müller 2019), some fundamental questions are still unanswered. How the accretion disks are supplied with external gas? Whether dose all the inflowing gas reach at accretion disk? Where is the inflowing gas originated from? The answers are benefit to comprehend the feed and feedback mechanisms and processes of quasars. Therefore, the observational evidence of inflows at the dusty torus and smaller scales (less than several tens of parsec) is crucial to study the process of SMBH accretion. Cold clouds in outflows, winds, or surrounding CGMs will condense and fall back toward central regions, providing material for broad emission line regions and central black holes (e.g., Gaspari et al. 2013; Li & Bryan 2014; Elvis 2017; Gaspari & Sądowski 2017). Many previous works have suggested inflowing clouds in/around the broad emission line region of quasars (e.g., Hu et al. 2008; Ferland et al. 2009; Gaskell & Goosmann 2013, 2016; Grier et al. 2017). However, up to now, only a few cases (e.g., Hall et al. 2013; Shi et al. 2017; Zhang et al. 2017; Zhou et al. 2019) of inflowing gas at these scales have been reported through redshifted broad absorption lines (BALs), where the BALs are defined as the absorption features hosting continual absorption features with line widths > 2000 km s⁻¹ at depths > 10% below the continuum

(Weymann et al. 1979), and are likely close to the equatorial plane of accretion disk. In addition, it is vacant up to now that the unambiguously observational evidence of inflowing gas is detected through metal narrow absorption line systems (NALs) in quasar spectra, where the NALs are the absorption features with line widths less than a few km s^{-1} , and are likely along the directions close to the axes of accretion disks (Hamann et al. 2012). In theory, clouds with enough column density of gas, which intercept quasar sightlines, could leave absorption features in quasar spectra. If the absorbing gas cloud falls towards the quasar central region (accretion disk), we can observe inflowing (redshifted) absorption features. This vacantness of the redshifted metal NALs can be ascribed to several factors. The first one is the quasar systemic redshift, which should be robust and accurate. If the quasar redshift is determined from broad emission lines, especially from the highly ionized C IV, there may be a large uncertainty in the quasar redshift (e.g., Shen et al. 2011), which often leads to misidentification of inflowing NALs. The second factor is that a NALs should be identified through at least 3 robust narrow absorption lines at the same redshift, which significantly reduces the sample size of NALs. If a NALs is only confirmed through the N v $\lambda\lambda 1238, 1242$, C IV $\lambda\lambda 1548, 1551$, or Mg II $\lambda\lambda 2796, 2803$ resonance doublet, the probability of false absorption line systems cannot be ignored. The third factor is that the radiation from quasar central regions is strong along the directions close to the axes of accretion disks. Most of the inflowing gas clouds, which are expected to produce NALs and along the directions close to the axes of accretion disks, are likely transformed into outflows by the strong quasar radiation when they reach hundreds of gravitational radii from SMBHs (Gaspari & Sądowski 2017). This would significantly reduce the incidence of inflowing NALs. Therefore, the inflowing NALs with high significant level are very difficult to be identified.

Here we report a sample of 9 redshifted narrow absorption line systems, whose upper limits of locations are around the dusty tori. The inflowing NALs possibly provide direct evidence for cold gas precipitation and accretion in AGN feedback processes, and provide the first direct evidence of inflowing gas along the directions close to quasar jets and at parsec scale. In this paper, we adopt the Λ CDM cosmology with $\Omega_M = 0.3$, $\Omega_\Lambda = 0.7$, and $H_0 = 70 \text{ km s}^{-1} \text{ Mpc}^{-1}$.

2. Data sample and spectral analysis

We aim to study quasar inflows through narrow absorption lines imprinted in quasar spectra. Therefore, we firstly select Mg II NALs with $v_r < 0$ from the largest catalog of quasar Mg II associated absorption lines (Chen et al. 2018a), which were detected from about 10^5 quasar spectra of the Sloan Digital Sky Survey (SDSS, Pâris et al. 2017). Here

$$v_r = c \times \frac{(1 + z_{em})^2 - (1 + z_{abs})^2}{(1 + z_{em})^2 + (1 + z_{abs})^2}, \quad (1)$$

where the z_{abs} is the absorption line redshift, the z_{em} is the quasar systemic redshift, and the c is the speed of light. Generally speaking, an absorber with $v_r < 0$ means that it is likely falling into quasar center region. The z_{abs} , which is measured from the narrow absorption line, is accurate. While, due to some mechanisms, such as quasar outflow,

the z_{em} , which is determined from quasar emission lines, is usually less than the true value. Therefore, it requires accurate quasar systemic redshift to define an inflow absorber by the velocity offset between z_{em} and z_{abs} . The quasar systemic redshift determined from narrow emission lines, such as [O II], is more accurate than that estimated from broad emission lines. Therefore, we further limit absorber sample to the Mg II NALs, which were detected in the quasar spectra shown obvious [O II] emission features. Meanwhile, we determine all the quasar systemic redshifts by fitting the [O II] emission features.

Chen et al. (2018a) identified a Mg II absorption line system only by the Mg II $\lambda\lambda 2796, 2803$ doublet. Only two absorption lines detected at the same redshift may lead to some false Mg II absorption line systems. In order to enhance the reliability of Mg II absorption line systems, we require that: (1) except for the Mg II $\lambda\lambda 2796, 2803$ doublet, one absorption system has at least two absorption lines at other rest-frame wavelengths that are detected at the same redshift, such as the series of absorption lines of Fe II, the Mg I $\lambda 2852$; and (2) the absorption line strengths with $W_r^{\lambda 2796} > 5\sigma_{W_r^{\lambda 2796}}$ and $W_r^{\lambda 2803} > 3\sigma_{W_r^{\lambda 2803}}$.

In term of the criteria mentioned above, we find that there are 9 Mg II NALs with $v_r < -1000 \text{ km s}^{-1}$ in the absorption line catalog of Chen et al. (2018a). Redshifted Mg II NALs can be originated from (1) measured errors of both the absorption line and emission line redshifts, due to the dispersions of absorption and emission lines; (2) [O II] emission line redshifts that cannot well represent the quasar systemical redshifts, since gas flows within emission line region may lead to an asymmetrical line profile; (3) the Mg II NALs formed within the external galaxies that are randomly moving in a cluster with large mass. The absorption features of all the 9 Mg II $\lambda\lambda 2796, 2803$ doublets are very significant and have good line profiles. In addition, two lines of all the Mg II $\lambda\lambda 2796, 2803$ doublets are clearly resolved with each other, and their line widths (σ_{abs}) are significantly less than 200 km s^{-1} . Therefore, the absorption redshifts (z_{abs}) of the Mg II NALs with $v_r < -1000 \text{ km s}^{-1}$ determined from the Mg II $\lambda\lambda 2796, 2803$ doublets are accurate. We determine the quasar systemic redshifts through [O II] $\lambda 3728$ narrow emission lines, which have line widths (σ_{eml}) about 300 km s^{-1} . Furthermore, both of the Mg II and [O II] emission lines have symmetrical profiles for all the quasars with redshifted Mg II NALs. In other words, we don't observe obvious outflow features in the broad Mg II and narrow [O II] emissions. Therefore, the quasar redshifts (z_{em}) determined from [O II] are robust. Relative to the [O II] emission lines, the velocity offsets of the 9 redshifted Mg II NALs are $v_r = 1071 - 1979 \text{ km s}^{-1}$, which are significantly larger than the uncertainty (σ_{drift}) contributed from line dispersions of the Mg II NALs and [O II] emission lines ($\sigma_{drift} = \sqrt{\sigma_{abs}^2 + \sigma_{eml}^2} = \sqrt{200^2 + 300^2} = 360 \text{ km s}^{-1}$). Therefore, the large velocity offsets ($v_r < -1000 \text{ km s}^{-1}$) of the 9 redshifted Mg II NALs are less likely originated from line dispersions.

It is well accepted that the quasar resides within a host galaxy, which is surrounded by circumgalactic medium (CGM). In addition, the quasar host galaxy would be a member galaxy of a galaxy cluster. Absorption lines would be imprinted in the quasar spectra, when the quasar center emission passes through its surrounding gas clouds located within an outflow, inflow, host galaxy, CGM, and

intergalactic medium (IGM) of the galaxy cluster before it reaches the observer. Therefore, a clustering distribution of absorption systems is often detected around the quasar emission redshift relative to the cosmological absorptions (e.g., Nestor et al. 2008; Wild et al. 2008; Chen et al. 2015, 2018a). We reanalyze the velocity distribution of Mg II NALs included in (Chen et al. 2018a), after cutting their quasars with $z_{\text{em}} < 1.07$ so that the quasar redshifts can be better determined from emission lines (e.g., Chen et al. 2018b). This cut reduces the numbers of Mg II NALs from 17,316 of Chen et al. (2018a) to 6349 of this paper. The velocity distribution of these 6349 Mg II NALs is shown in Figure 1, which clearly shows that there is an significantly excess around $v_r \approx 0$. This suggests that the Mg II absorptions would be clustered around quasars. In addition, Figure 1 also implies that velocity distribution of Mg II absorbers is complex, and the absorber sample should include absorptions that originated in the quasar’s outflow, inflow, surrounding environment, and foreground intervening galaxies. The intervening absorbers should have a uniform random velocity distribution at $v_r > 0$. The environmental absorbers should have a normal velocity distribution at $v_r = 0$, which is destroyed by the outflow absorbers at blue wing ($v_r > 0$). The extended red wing of Figure 1 ($v_r < 0$) is likely originated from inflow absorbers. Accounting for the multiple components of the velocity distribution, we invoke three Gaussian functions to describe velocity distributions of the outflow (Gaussian center $v_r > 0$), environment (Gaussian center $v_r = 0$), and inflow (Gaussian center $v_r < 0$) absorbers, and invoked a linear function with slope $\alpha = 0$ to characterize the velocity distribution of the intervening absorbers. The results are exhibited with color lines in Figure 1, which clearly shown that all the inflow, environmental, and outflow absorbers are mixed in the velocity range of $v_r < 0$. In addition, both the environment and outflow Mg II NALs are limited within $v_r > v_0 - 3\sigma > -1000 \text{ km s}^{-1}$, where the v_0 and σ are the Gaussian function fitting centers and dispersions, respectively. Therefore, the “ $v_r < -1000 \text{ km s}^{-1}$ ” is a good velocity cut to select the true inflow absorbers, which can well eliminate the contamination from the environment/outflow absorptions. Thus, the 9 redshifted Mg II NALs with $v_r < -1000 \text{ km s}^{-1}$ are statistically unlikely to be formed within outflow or the external galaxies (environment) that are randomly moving in a cluster, but they are likely truly inflowing towards quasar central regions.

In term of the discussions mentioned above, the 9 redshifted Mg II NALs with $v_r < -1000 \text{ km s}^{-1}$ are likely originated within the inflowing material. We show the spectra of the 9 redshifted Mg II NALs with $v_r < -1000 \text{ km s}^{-1}$ in Figures 2 and 3. For all these 9 redshifted Mg II NALs with $v_r < -1000 \text{ km s}^{-1}$, we also measure the absorption strengths of the Mg I $\lambda 2852$, the series of Fe II, and the CIV $\lambda \lambda 1548, 1551$ when available. The results are listed in Table 1.

In order to measure the black hole mass and bolometric luminosities of quasars, we further analyze the quasar spectra. All the quasar spectra are corrected for the Galactic extinction using the Reddening measurements of Schlafly & Finkbeiner (2011) and Milky Way extinction curve from Cardelli et al. (1989). We fit local power-law continuum ($f_\lambda = A\lambda^\alpha$) plus iron template (Vestergaard & Wilkes 2001) using the spectra data around the Mg II emission lines and not contaminated by the con-

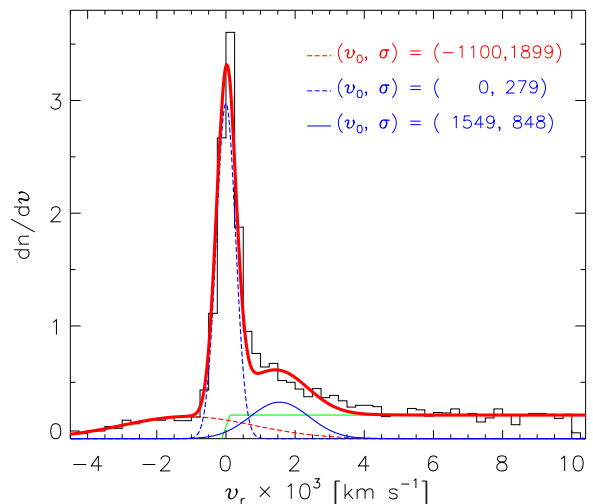


Fig. 1. Relative velocity distribution of 6349 Mg II NALs with $z_{\text{em}} < 1.07$. The data are directly taken from the 17,316 Mg II NALs of Chen et al. (2018a). The red dashed, blue dashed, and blue solid curves indicate the Gaussian function fits, which correspond to inflow, environment, and outflow Mg II NALs, respectively. The green solid line indicates the mean count at $v_r > 6000 \text{ km s}^{-1}$, which corresponds to intervening Mg II NALs. The red solid curve is the sum of all the color lines. The values shown in the top right corner are the Gaussian function fitting centers (v_0) and dispersions (σ).

sidering line emissions. See Figures 2 for the fitting results. The Mg II emission line properties are measured from the spectra subtracted by the continuum+iron fits. We invoked two Gaussian functions to fit the Mg II emission features, of which one having FWHM $> 1200 \text{ km s}^{-1}$ (e.g., Shen et al. 2011; Chen et al. 2019) is for the broad Mg II component, and the other one, whose FWHM is determined from the [O II] emission lines, is for the narrow Mg II component. During the fits of emission lines, we exclude the spectral data around the strong Mg II $\lambda \lambda 2796, 2803$ absorption doublets. We derive the black hole mass M_{BH} of the quasar via

$$\text{Log}\left(\frac{M_{\text{BH}}}{M_\odot}\right) = a + b \times \text{Log}\left(\frac{L_{3000}}{10^{44} \text{ erg s}^{-1}}\right) + 2 \times \text{Log}\left(\frac{\text{FWHM}_{\text{Mg II}}}{\text{km s}^{-1}}\right), \quad (2)$$

where the calibrated coefficients (a, b) = (0.82, 0.5) are empirical values (e.g., Chen et al. 2019), and the L_{3000} is the monochromatic luminosity of the quasar at 3000 Å, which is estimated from the fitting power-law. The bolometric luminosity of quasar is directly derived from the monochromatic luminosity with standard bolometric correction, namely, $L_{\text{bol}} = 5.15 L_{3000}$ (Richards et al. 2006). We also estimate the mass accretion rate of black hole by $\dot{M}_{\text{BH}} = \frac{L_{\text{bol}}}{\epsilon c^2}$, where $\epsilon = 0.1$ is the mass-to-radiation conversion efficiency. The Eddington ratio can be derived from $\eta = L_{\text{bol}}/L_{\text{Edd}}$, where the Eddington luminosity $L_{\text{Edd}} = 1.38 \times 10^{38} (M_{\text{BH}}/M_\odot) \text{ erg s}^{-1}$. The resulting L_{3000} , M_{BH} , \dot{M}_{BH} , and η are provided in Table 2.

3. The results and discussions

In the following, we discuss the properties of locations, mass inflow rates, radio emissions, and origins for the 9 redshifted Mg II NALs with $v_r < -1000 \text{ km s}^{-1}$.

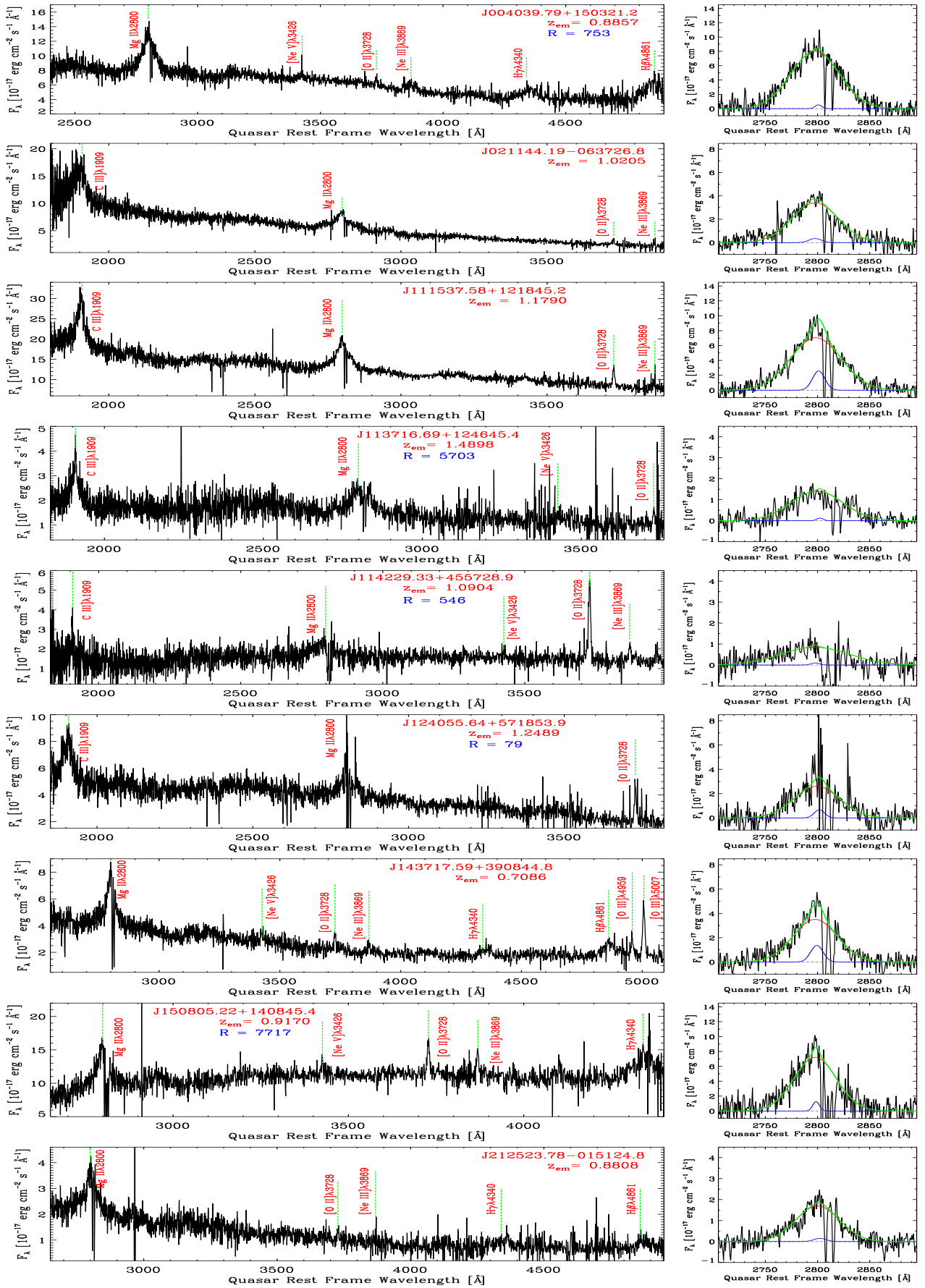


Fig. 2. The SDSS quasar spectra. Left panel: Green dash-lines indicate the positions of emission lines. The emission line redshifts z_{em} are determined from the [O II] emission lines. The blue symbols are the radio loudness of quasars: $R = \frac{f_{6cm}}{f_{2500}}$. Right panel: The quasar spectra have been subtracted by the continuum+iron fits. The blue and red lines are the narrow and broad Gaussian function fits, respectively. The green lines are the sum of the blue and red lines.

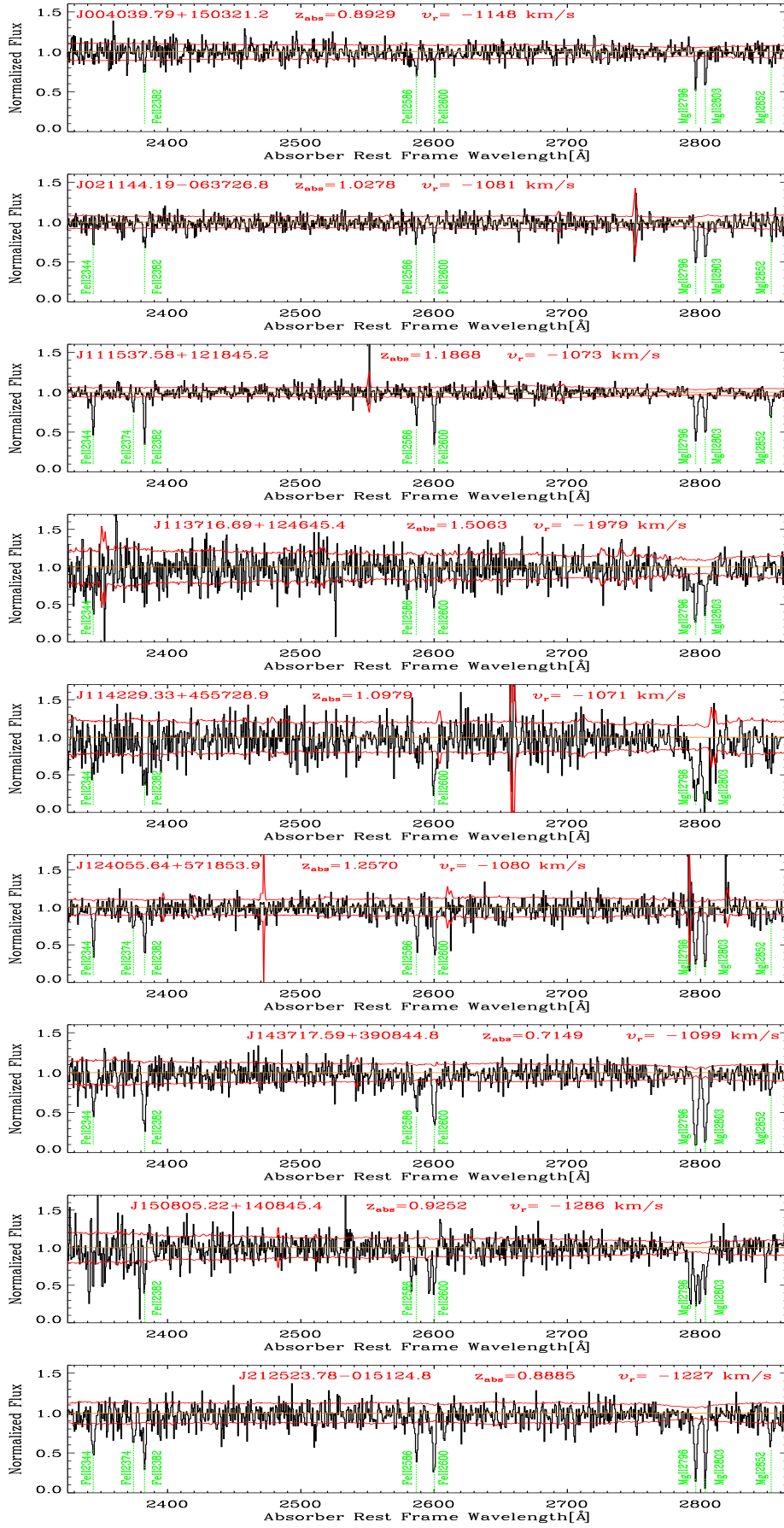


Fig. 3. The quasar spectra normalized by fitting continuum. The red lines are the $\pm 1\sigma$ flux uncertainty levels, which have also been normalized by the fitting continuum. Green dash-lines label the obvious absorption lines located at the same z_{abs} , where the values of z_{abs} are in the top of each figure.

Table 1. The measurements of absorption lines

SDSS NAME	z_{abs}	$W_r^{\lambda 2796}$ Å	$W_r^{\lambda 2803}$ Å	$W_r^{\lambda 2852}$ Å	$W_r^{\lambda 2600}$ Å	$W_r^{\lambda 2586}$ Å	$W_r^{\lambda 2382}$ Å	$W_r^{\lambda 2374}$ Å	$W_r^{\lambda 2344}$ Å	$W_r^{\lambda 1548}$ Å	$W_r^{\lambda 1551}$ Å
(1)	(2)	(3)	(4)	(5)	(6)	(7)	(8)	(9)	(10)	(11)	(12)
004039.79+150321.2	0.8929	0.65±0.07	0.69±0.08	0.42±0.18	0.36±0.09	0.68±0.20	0.44±0.17	—	—	—	—
021144.19-063726.8	1.0278	1.13±0.13	0.98±0.16	0.32±0.10	0.45±0.13	0.41±0.10	0.72±0.18	—	0.38±0.09	—	—
111537.58+121845.2	1.1868	1.47±0.07	1.17±0.07	0.68±0.09	1.15±0.10	0.68±0.09	1.00±0.08	0.40±0.09	0.93±0.09	—	—
113716.69+124645.4	1.5063	2.02±0.22	1.49±0.21	—	1.06±0.31	0.41±0.20	—	—	1.01±0.33	0.57±0.17	0.22±0.10
114229.33+455728.9	1.0979	3.99±0.69	4.64±0.75	—	2.51±0.72	—	2.90±0.94	—	1.30±0.51	—	—
124055.64+571853.9	1.2570	2.04±0.20	1.86±0.19	0.57±0.22	1.58±0.28	1.28±0.27	1.29±0.19	0.57±0.19	1.27±0.18	—	—
143717.59+390844.8	0.7149	3.40±0.21	2.88±0.21	0.72±0.26	2.20±0.32	1.34±0.29	2.25±0.42	—	1.50±0.43	—	—
150805.22+140845.4	0.9252	1.92±0.14	1.54±0.17	—	1.42±0.27	0.76±0.30	1.07±0.31	—	—	—	—
212523.78-015124.8	0.8885	2.24±0.19	1.99±0.17	1.09±0.36	2.02±0.27	1.48±0.29	1.79±0.35	0.98±0.30	1.38±0.31	—	—

Note. (1) The SDSS name of quasars; (2) The redshift of Mg II NALs; (3)—(12) The equivalent widths of Mg II $\lambda\lambda 2796, 2803$, Mg I $\lambda 2852$, Fe II $\lambda 2600$, Fe II $\lambda 2586$, Fe II $\lambda 2382$, Fe II $\lambda 2374$, Fe II $\lambda 2344$, Cr V $\lambda\lambda 1548, 1551$ absorption lines. The “—” means no detection.

Table 2. The parameters of quasars and absorption line systems

SDSS NAME	z_{em}	z_{abs}	v_r km s ⁻¹	R	C_f	$\text{Log}L_{3000}$ erg s ⁻¹	$\text{Log}M_{\text{BH}}$ M_{\odot}	η	\dot{M}_{BH} M_{\odot}/yr	R_{BELR} pc	R_{torus} pc	R_{NELR} pc	$R_{\text{abs}}^{\text{HG}}$ pc	$R_{\text{abs}}^{\text{BH}}$ pc
(1)	(2)	(3)	(4)	(5)	(6)	(7)	(8)	(9)	(10)	(11)	(12)	(13)	(14)	(15)
004039.79+150321.2	0.8857	0.8929	-1148	753	0.52	45.33	9.06	-1.131	1.96	0.126	1.595	493.30	12.46	7.53
021144.19-063726.8	1.0205	1.0278	-1081	—	0.53	45.16	8.84	-1.081	1.31	0.144	1.304	376.59	7.26	5.06
111537.58+121845.2	1.1790	1.1868	-1073	—	0.60	45.79	9.08	-0.698	5.53	0.219	2.682	990.42	16.05	8.99
113716.69+124645.4	1.4898	1.5063	-1979	5703	0.81	45.19	8.95	-1.170	1.37	0.104	1.333	388.21	1.48	1.94
114229.33+455728.9	1.0904	1.0979	-1071	546	0.84	44.85	8.81	-1.367	0.64	0.069	0.909	232.25	6.67	4.83
124055.64+571853.9	1.2489	1.2570	-1080	79	0.82	45.43	8.89	-0.862	2.46	0.142	1.788	575.15	8.04	5.76
143717.59+390844.8	0.7086	0.7149	-1099	—	0.93	44.60	8.33	-1.129	0.36	0.054	0.684	158.76	1.70	1.50
150805.22+140845.4	0.9170	0.9252	-1286	7717	0.77	45.42	8.70	-0.689	2.37	0.140	1.755	560.78	2.78	2.62
212523.78-015124.8	0.8808	0.8885	-1227	—	0.83	44.57	8.28	-1.123	0.34	0.042	0.662	151.97	1.04	1.09

Note. Column (4): Relative velocities of absorbers with respect to quasar emission line redshifts; (5) $R = \frac{f_{6cm}}{f_{2500}}$, which represents the radio loudness of quasars; (6) The coverage fraction of the Mg II absorbing cloud relative to the continuum emission region; (7) The monochromatic luminosity of the quasar at 3000 Å; (8) The mass of the black hole; (9) The Eddington ratio $\eta = L_{\text{bol}}/L_{\text{Edd}}$; (10) The mass accretion rate of the black hole; (11) The size of the broad emission line region; (12) The inner radius of dusty torus; (13) The size of the narrow emission line region; (14) The largest distances of absorbers from central SMBH, considering the gravitational potential contributed by the central supermassive black hole and a Hernquist stellar distribution for the hosting galaxy (Hernquist 1990); (15) The largest distances of absorbers from central SMBH, only considering the gravitational field of central SMBH.

3.1. The locations of infalling absorbers

We estimate the locations ($R_{\text{abs}}^{\text{HG}}$) of these inflowing NALs assuming that they are initially formed in the hosting galaxies and then fall freely toward the center. Due to the drag force from the surrounding hot gas, the centrifugal force and the potential radiation pressure from the central source, the true line-of-sight velocities of inflowing NALs should be less than the free-fall velocities. Therefore, our estimated values are an upper limit for $R_{\text{abs}}^{\text{HG}}$. We consider the gravitational potential contributed by the central supermassive black hole and a Hernquist stellar distribution for the bulge of the hosting galaxy (Hernquist 1990). The bulge stellar mass M_* is derived from the black hole mass M_{BH} from the $M_{\text{BH}} - M_*$ relation given by Häring & Rix (2004),

$$\frac{M_{\text{BH}}}{M_{\odot}} = 1.6 \times 10^8 \left(\frac{M_*}{10^{11} M_{\odot}} \right)^{1.12}, \quad (3)$$

and the effective radius R_e of the bulge stellar distribution is then determined from the observational $R_e - M_*$ relation

for early-type galaxies in Shen et al. (2003),

$$R_e = 2.88 \times 10^{-6} \left(\frac{M_*}{M_{\odot}} \right)^{0.56} \text{ kpc}. \quad (4)$$

We then calculate the values of $R_{\text{abs}}^{\text{HG}}$ assuming that the free-fall velocities of the gas clouds reach the observed inflowing velocities at $R_{\text{abs}}^{\text{HG}}$ in this potential well. The resulting distances of our inflowing absorbers $R_{\text{abs}}^{\text{HG}}$ are provided in Table 2. We find that the derived values of $R_{\text{abs}}^{\text{HG}}$ for our 9 inflowing Mg II NALs are all roughly $2 \times 10^4 R_g - 2 \times 10^5 R_g$, substantially lower than the radius of the sphere of the influence of the central SMBHs ($\sim 10^6 R_g$ assuming a representative bulge stellar velocity dispersion of ~ 200 km/s, Netzer 2015).

If considering the inflowing NALs are initially formed around dusty tori, the inflowing gas clouds are dominated by the gravitational field of the central SMBH. In this case, the resulting distances of inflowing absorbers $R_{\text{abs}}^{\text{BH}}$ are lightly smaller than the $R_{\text{abs}}^{\text{HG}}$. The resulting $R_{\text{abs}}^{\text{BH}}$ are also listed in Table 2.

Using the radius-luminosity relations, we derive the sizes of broad emission line regions (R_{BELR} , Bentz et al. 2013)

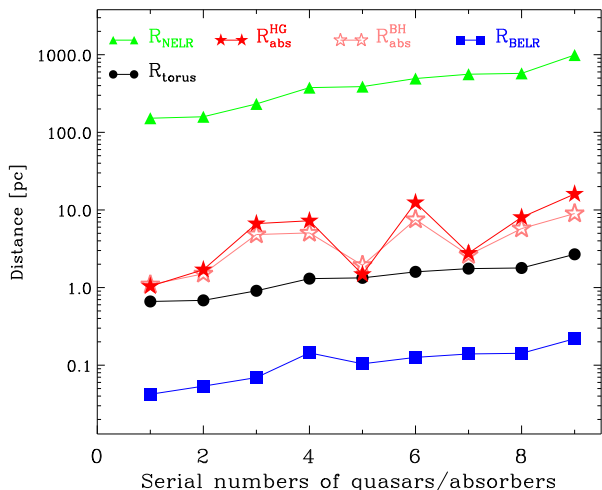


Fig. 4. The distances of the broad emission line region (R_{BELR}), dusty torus (R_{torus}), narrow emission line region (R_{NELR}), and inflow cloud ($R_{\text{abs}}^{\text{HG}}$ or $R_{\text{abs}}^{\text{BH}}$) from the quasar central region. The $R_{\text{abs}}^{\text{HG}}$ considers the gravitational potential contributed by the central supermassive black hole and a Hernquist stellar distribution for the bulge of the hosting galaxy (Hernquist 1990), and the $R_{\text{abs}}^{\text{BH}}$ only considers the gravitational field of central SMBH.

and narrow emission line regions (R_{NELR} , Mor & Netzer 2012), and the inner radius of dusty torus (R_{torus} , Nenkova et al. 2008) from quasar luminosities. The resulting in R_{BELR} , R_{NELR} , and R_{torus} are shown in Figure 4 and also listed in Table 2. It is clearly seen from Figure 4 that the R_{abs} is just slightly larger than the inner radius of dusty torus R_{torus} , implying that the infalling Mg II NALs could be formed within the gas clouds located near the dusty tori.

3.2. The mass inflow rates

Assuming a simplest model that the infalling Mg II NALs is formed within a discrete clouds (Zhou et al. 2019), we can estimate the mass inflow rate via

$$\dot{M}_{\text{inflow}} = \mu m_{\text{p}} N_{\text{H, inflow}} f_{\text{f}} 4\pi d_{\text{inflow}}^2 \Omega_{\text{inflow}} / t_{\text{inflow}} \quad (5)$$

where $\mu = 1.4$ is the mean atomic mass per proton, m_{p} is the mass of a proton, $N_{\text{H, inflow}}$ is the column density of neutral hydrogen within the inflow cloud, f_{f} is the filling factor of the absorbing clouds, the in-falling distance d_{inflow} equals to the distance R_{abs} of the absorbing cloud, Ω_{inflow} is the global covering factor of the inflow structure, and t_{inflow} is the in-falling timescale. Considering the gravitation and radiation pressure from central region, the infalling timescale of the inflow absorber $t_{\text{inflow}} \approx d_{\text{inflow}} / v_{\text{inflow}}$ when the absorber is falling towards central black hole from the observed distance, where v_{inflow} equals to the relative velocity v_r of the Mg II NALs measured from quasar spectra. The filling factor f_{f} may be the same order as the effective coverage fraction C_{f} of the absorbing cloud to background emission sources for the BALs (Zhou et al. 2019). However, the f_{f} may be much smaller than the C_{f} for the NALs. In this paper, we only estimate the upper limit of the mass inflow rate from Equation (5), therefore, we still consider $f_{\text{f}} = C_{\text{f}}$. This would not change our result.

Among 9 redshifted Mg II NALs with $v_r < 1000 \text{ km s}^{-1}$, the high ionization C IV absorption is only available for one

system, and we only detect the Mg^+ and Fe^+ iron absorption lines for the other 8 systems with available spectra. The hydrogen column density (N_{H}) of the inflowing absorbers cannot be well determined by the photoionization simulations (Ferland et al. 2017) if the Mg^+ and Fe^+ iron absorption lines are only available, since both the Mg^+ and Fe^+ irons have similar ionization potential. As a matter of fact, the metal BALs and DLAs (damped $\text{Ly}\alpha$ absorption line systems) often host a hydrogen column density significantly larger than 10^{20} cm^{-2} , and the metal NALs usually have $N_{\text{H}} < 10^{20} \text{ cm}^{-2}$. Here we assume $N_{\text{H}} = 10^{20} \text{ cm}^{-2}$ for all the 9 inflowing Mg II NALs to estimate the upper limit of mass inflow rates.

The absorption line intensity ($I(v)$), which has been normalized by the background radiations, is a function of the optical depth ($\tau(v)$) and the effective coverage fraction ($C_{\text{f}}(v)$) of the absorbing cloud to background emission sources. That is,

$$I(v) = [1 - C_{\text{f}}(v)] + C_{\text{f}}(v)e^{-\tau(v)}. \quad (6)$$

For the Mg II $\lambda\lambda 2796, 2803$ doublet that has an optical depth ratio of 2 : 1, we assume that C_{f} is the same for both lines. Therefore, we can obtain

$$C_{\text{f}}(v) = \frac{[I_r(v) - 1]^2}{I_b(v) - 2I_r(v) + 1}. \quad (7)$$

Considering the resolution of the SDSS spectra $R = \Delta\lambda/\lambda \approx 1800$ and line profile of narrow absorption line, we only derive the effective coverage fraction of the absorbing cloud using the normalized intensities at line cores. The results are provided in Table 2. Note that the C_{f} is only used to estimate the mass inflow rate (see Equation (5)). In the following comparison (see Figure 5), we will see that an accurate C_{f} cannot change the results, and the \dot{M}_{inflow} is still much less than the \dot{M}_{BH} , even if we adopt $C_{\text{f}} = 1$.

With the $N_{\text{H}} = 10^{20} \text{ cm}^{-2}$, C_{f} , R_{abs} , and v_r being available/given, we can obtain $\dot{M}_{\text{inflow}} = (0.0183 - 0.2478)\Omega_{\text{inflow}} M_{\odot}/\text{yr}$ for our 9 infalling Mg II NALs from Equation 5, where the $\Omega_{\text{inflow}} < 1$. Figure 5 compares the mass accretion rate of black hole and the mass inflow rate of absorbing gas for different Ω_{inflow} values. It is clearly seen that $\dot{M}_{\text{inflow}} \ll \dot{M}_{\text{BH}}$, suggesting that the infalling NALs cannot provide sufficient fuels to power the quasars.

3.3. The properties of Radio emissions

We collect quasar emission data at radio-bands through the High Energy Astrophysics Science Archive Research Center Online Service, provided by the NASA/Goddard Space Flight Center. We find that all of these 9 quasars are lied within the footprint of the Faint Images of the Radio Sky at Twenty cm (FIRST). Therefore, firstly, we match our quasar sample to FIRST using a $5''$ matching radius, which results in 5 quasars with the FIRST detections. Secondly, we match the 5 quasars with the FIRST detections to other catalogs of radio observations using a $60''$ matching radius. We find that, except for the 20 cm observations, there are 4 quasars being observed at other radio frequencies. For the quasars with the FIRST detection within a $5''$ matching radius, we also match the quasars with the FIRST catalog using a $60''$ matching radius. Within a $60''$ matching radius, the quasars only with one counterpart of the FIRST

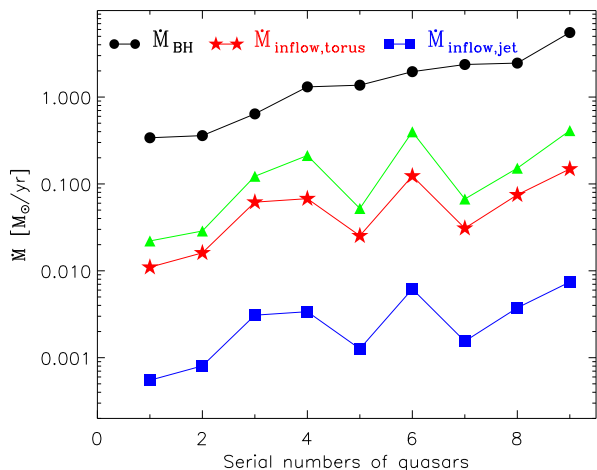


Fig. 5. The mass accretion rate of the central black hole (black circles) and the mass inflow rate of absorbing gas (color symbols). Red stars are for $\Omega_{\text{inflow}} = 0.6$ (dusty torus), blue squares are for $\Omega_{\text{inflow}} = 0.03$ (back flow), and green triangles are for $\Omega_{\text{inflow}} = 1$ and $C_f = 1$.

are likely to be core-dominated sources, and those with at least two counterparts of the FIRST are likely to be lobe-dominated sources (e.g., Shen et al. 2011). Based on this criterion, we find that 3 quasars are core-dominated sources among the 5 quasars with the FIRST detections. This indicates that most of the quasars with the FIRST detections are likely observed along the directions close to the axes of accretion disks (with small inclination angles), which are the directions at which the NALs associated with quasar outflows/winds were observed (Hamann et al. 2012).

We also compute the radio loudness of quasars via

$$R = \frac{f_{6 \text{ cm}}}{f_{2500}}, \quad (8)$$

where the $f_{6 \text{ cm}}$ and f_{2500} are the flux density (f_ν) at 6 cm and 2500 Å, respectively. The f_{2500} is directly taken from the fitting pow-law continuum of quasars at 2500 Å. The flux density at rest-frame 6 cm is estimated from multi-band measurements using the fitted power-law spectral index, otherwise is from the only available FIRST 20 cm observations assuming a spectral index of 0.5. During the power-law fits in radio-bands, we adopt the total flux of all the components for the two lobe-dominated sources. We note that the observations at different radio bands were done at different resolutions, which may yield a different flux at the same frequency for the same one source, especially for the extended sources. Except for the FIRST detection (at a resolution of 5''), the radio observations from other surveys were done at much lower resolutions ($\geq 45''$). Here, we compare the fluxes at 1.4 GHz obtained by the FIRST (at a resolution of 5'') and the National Radio Astronomy Observatory Very Large Array Sky Survey (NVSS, Condon et al. 1998, at a resolution of 45''), respectively. We find that the fluxes obtained by the FIRST are similar to those obtained by the NVSS, which indicates that the resolutions of observations would not yield significant difference in the calculations of radio indices.

The resulting in R from Equation 8 are listed in Table 2. We find that $R = 79, 546, 753, 5703,$ and 7717 for the 5 quasars with the FIRST detections, which are within the

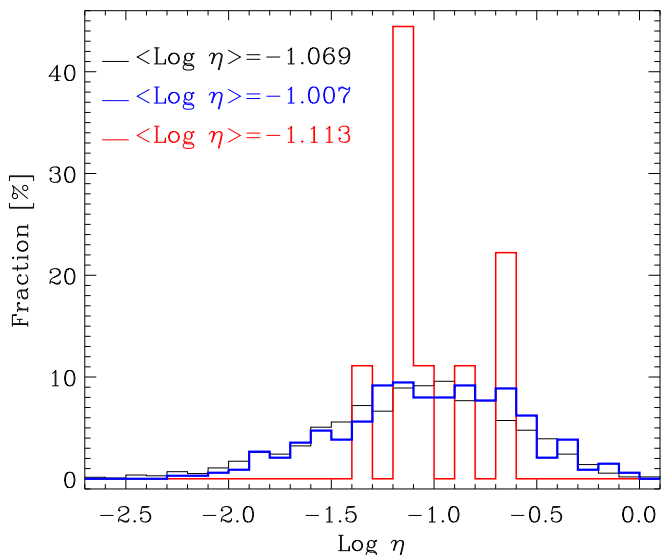


Fig. 6. Distributions of the Eddington ratios η of quasars. The black solid-line is for all the quasars with $z_{\text{em}} < 1.07$ (2724 quasars), whose black hole mass can be available from previous works. The median value is $\langle \text{Log} \eta \rangle = -1.069$. The blue solid-line is for the quasars with outflow Mg II NALs (338 quasars), whose median value is $\langle \text{Log} \eta \rangle = -1.007$. The red solid-line is for the 9 quasars with inflowing Mg II NALs, whose median value is $\langle \text{Log} \eta \rangle = -1.113$.

range covered by blazars (e.g., Fan et al. 2011; Pei et al. 2019, 2020). The radio loudness of quasars suggests that the 5 quasars with the FIRST detected are likely Blazars, which further supports that these sources are likely observed along the directions close to the axes of accretion disks.

3.4. The Eddington ratios

The Eddington ratios of the 9 quasars with inflowing Mg II NALs are shown with red solid-line in Figure 6. We calculate the Eddington ratios for all the quasars with $z_{\text{em}} < 1.07$, included in Chen et al. (2018a), when their black hole mass can be available from previous works (e.g., Shen et al. 2011; Chen et al. 2018b, 2019). The results are shown with black solid-line in Figure 6, which includes 2724 quasars. It is clearly seen from Figure 1 that the Mg II NALs with $3 * 279 < v_r < 1549 + 848 \text{ km s}^{-1}$ would be dominated by outflow absorptions, where the 279 km s^{-1} is the velocity dispersion of the environmental absorptions (the blue dash-line in Figure 1), the 1548 km s^{-1} is the central velocity of the outflow absorptions (the blue solid-line in Figure 1), and the 848 km s^{-1} is the velocity dispersion of the outflow absorptions. There are 338 quasars, whose Mg II NALs fall into the velocity range of $3 * 279 < v_r < 1549 + 848 \text{ km s}^{-1}$. Here these 338 quasars are considered as the sources with outflow Mg II NALs, whose Eddington ratios are shown with blue solid-line in Figure 6. It is clearly seen from 6 that, on average, the quasars with inflowing Mg II NALs have a slightly smaller Eddington ratio relative to those with outflow Mg II NALs. It can be seen from Figure 1 that the outflow component (blue solid-line) is significantly contaminated by the intervening absorptions (green solid-line) in the velocity range of $3 * 279 < v_r < 1549 + 848 \text{ km s}^{-1}$. Therefore, above definition of quasars with outflow Mg II NALs would significantly reduce the purity of sample of

quasars with outflow Mg II NALs. The Eddington ratios of the quasars with confirmed outflow Mg II NALs might be on average larger than those shown with blue solid-line in Figure 6. Thus, Figure 6 provides a hint that the quasars with inflowing Mg II NALs may have a lower radiation pressure with respect to the sources with outflow Mg II NALs. In the future, we will further investigate whether the properties of inflow/outflow Mg II NALs depend on the intrinsic characteristics of quasars, when a large sample of quasars with confirmed outflow Mg II NALs is available.

4. The origins of infalling Mg II NALs

The upper limits of R_{abs} are around the regions of dusty tori. Therefore, one possible origin of the infalling Mg II NALs is that they are from dusty tori. Within the dusty tori, clouds have a Gaussian distribution along the angular direction, and is decreased in the way of $1/r$ or $1/r^2$ along the radial direction (Nenkova et al. 2008). Therefore, we assume a Gaussian distribution of the absorbing gas from accretion disk plane, when the infalling Mg II NALs are formed within the dusty tori. That is,

$$N_{\text{g}}(\beta) = N_0 e^{(-\beta^2/\sigma^2)}, \quad (9)$$

where N_{g} is the column density of gas cloud, N_0 is a normalized parameter, β is the angle between sightline and accretion disk plane, σ is a typical angle width of gas distribution, and the gas column density is a constant within the angle width $|\beta| \leq \sigma$, namely, $N_{\text{g}} = N_0$. Figure 7 shows the distribution of gas column density as a function of β for several σ . In this scenario, the BALs and NALs are observed along sightlines with small and large β , respectively, which are consistent with the model of Hamann et al. (2012). Assuming that $\sigma = 20^\circ$ and the infalling BALs of quasar J103516.20 + 142200.6 ($N_{\text{H}} = 10^{23.46} \text{ cm}^{-2}$, Zhou et al. 2019) was observed along the sightline with $\beta = 45^\circ$, we can constrain that our infalling Mg II NALs ($N_{\text{H}} = 10^{20} \text{ cm}^{-2}$) were observed along the directions with $\beta \approx 75^\circ$, which are quite close to the axes of accretion disks. Adopting $\Omega_{\text{inflow}} = 0.6$ (Zhou et al. 2019), we find that $\dot{M}_{\text{inflow}} = (0.0110 - 0.1487) M_{\odot}/\text{yr}$ if the infalling Mg II NALs are formed within dusty tori, which are about one order of magnitude lower than the accretion rates of black holes (see the red stars in Figure 5).

Alternatively, the infalling Mg II NALs may result from the interaction of AGN jets with the interstellar medium (ISM), which leads to cold gas precipitation and chaotic cold accretion onto central SMBHs (e.g., Gaspari et al. 2013; Li & Bryan 2014). The jet-ISM interaction leads to nonlinear development of local thermal instability, and cold gas precipitates and falls back to the central regions preferentially along the directions close to the jet axis. Simulations indicate that with this mechanism, a majority of the cold gas forms at kiloparsec and larger distances away from the central SMBH. The detected infalling NALs are located on the parsec scale along the sightlines quite close to the axes of accretion disks, and therefore they may be originally formed nearly along the jet axes on the kiloparsec scale. A natural place to form these cold gaseous blobs is metal-rich trailing outflows uplifted by the jet ejecta through the Darwin drift mechanism (Guo et al. 2018; Duan & Guo 2018). The initially hot or warm gas converges and cools rapidly in trailing outflows, and the resulted cold NALs experience a

transition from an initial outflowing stage to a later inflowing stage. The whole process is expected to last for about 100 Myr, long after the jet ejecta becomes undetectable at 20 cm. This picture is consistent with the rather high fraction (5/9) of the FIRST radio detection of our inflowing Mg II NALs. The NAL absorbers may thus provide direct evidence for cold gas precipitation and accretion in AGN feedback processes. In this picture, we expect that Ω_{inflow} is significantly lower than 1. Adopting $\Omega_{\text{inflow}} = 0.03$ that corresponds to a half-opening angle of 15° , we find that $\dot{M}_{\text{inflow}} = (0.0005 - 0.0074) M_{\odot}/\text{yr}$, which is about 2 – 3 orders of magnitude lower than the accretion rates of black holes (see the blue squares in Figure 5). These low mass inflow rates are consistent with the suggestions that the chaotic cold accretion cannot provide sufficient gas to trigger luminous quasars (e.g., Gaspari & Sądowski 2017; Storchi-Bergmann & Schnorr-Müller 2019).

In term of above discussions, it does not matter whether the infalling Mg II NALs are from the dusty tori or the chaotic cold accretion, the infalling NALs cannot provide sufficient fuels to power the quasars. Even if we adopt the upper limits of $C_{\text{f}} = 1$ and $\Omega_{\text{inflow}} = 1$, the mass inflow rate is still obviously less than the mass accretion rate of black hole (see the green triangles in Figure 5).

The inflowing gas of BALs, or most of them, moves mainly along the directions close to the equatorial plane, where the radiation flux from the central engine is relatively small. The BAL absorbers will thus experience weak radiation pressure and would be pulled onto accretion disks by the gravity of central SMBHs and provide materials to feed the growth of central SMBHs. However, the inflowing gas of NALs move mainly along the directions close to the rotational axis of accretion disks. Strong radiation flux exists along these directions. Therefore, the NAL absorbers are expected to be decelerated by the radiation pressure. They may even become outflows by the radiation line force although the quasar radiation is sub-Eddington (Proga 2007; Gaspari & Sądowski 2017). Therefore, the ultimate destiny of inflowing NALs is possibly different from that of inflowing BALs, where the inflowing BALs are transported to the accretion disks, and then to feed the SMBHs.

5. Summary

Using the large quasar catalog from the SDSS, this work aims to search for redshifted/infalling Mg II NALs, which is benefit to comprehend the feed and feedback mechanisms and processes of quasars. We obtain 9 robust Mg II NALs with $v_r < -1000 \text{ km s}^{-1}$, which are identified by Mg II $\lambda\lambda 2796, 2803$ doublet, and at least two absorption lines at other rest-frame wavelengths, such as the series of absorption lines of Fe II, and the CIV $\lambda\lambda 1548, 1551$. Every system is identified by more than four narrow absorption lines, which guarantees that our 9 Mg II NALs are reliable. Both the redshifts of the quasar (z_{em}) and absorption (z_{abs}) systems are determined by narrow lines, which guarantees the high accuracy of both the z_{em} and z_{abs} . In addition, the large inflowing speed ($v_r < -1000 \text{ km s}^{-1}$) ensures that our 9 Mg II NALs are much likely infalling towards quasar central regions. They are very unlikely to be originated in the external galaxies that are randomly moving in the cluster of quasar host galaxy, and much unlikely to be formed within the gas clouds located within the quasar host galaxy and CGM.

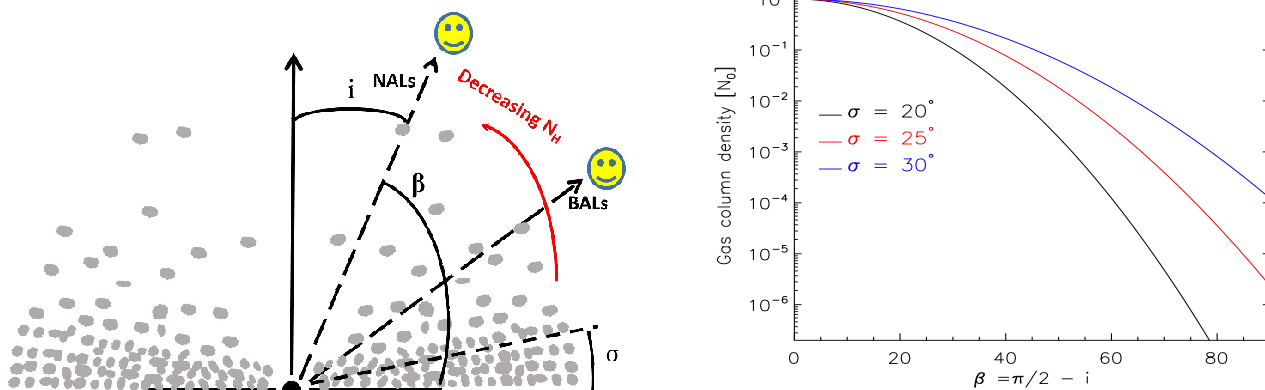


Fig. 7. Left panel: A cartoon for the distribution of the absorbing gas from accretion disk plane. i is the angle between sightline and axial direction of accretion disk, and $\beta = \frac{1}{2}\pi - i$. The gas column density is a constant within the angle width $|\beta| \leq \sigma$. The BALs would be possibly observed along sightline with small β , and the NALs would be possibly detected along the sightline with small i . Right panel: The gas column density as a function of β , giving an angle width σ .

The 9 redshifted Mg II NALs are infalling towards quasar central regions in speeds of $1071 - 1979 \text{ km s}^{-1}$, and located around the dusty tori (parsec scale from central SMBHs). Both the narrow line characteristic of absorption systems and strong radio emissions of quasars suggest that these redshifted Mg II NALs are likely along the directions close to the axes of accretion disks.

The quasars showing inflows might have lower radiation pressure when compared to the sources with outflows, which will be further studied when a large sample of quasars with confirmed outflow absorptions are available in the future.

Although we cannot confirm where the inflowing Mg II NALs come from with present data, there are two possible origins. One possible origin is that the inflowing Mg II NALs are formed within the dusty tori. The other one possibility is that the inflowing Mg II NALs are from the chaotic cold accretion resulted from the nonlinear interaction of AGN jets with the interstellar medium, where the cold gaseous blobs may originally precipitate in metal-rich trailing outflows uplifted by AGN jet ejecta. Therefore, our inflowing Mg II NALs might be the direct evidence of cold gas precipitation and accretion in AGN feedback processes, and the direct evidence of inflowing gas along the directions close to quasar jets and at parsec scale. Of course, we note that the mass inflow rates of the infalling Mg II NALs are much less than the mass accretion rates of black holes. Thus the infalling NALs cannot provide sufficient fuels to power the quasars.

Acknowledgements. Zhi-Fu Chen is supported by the Guangxi Natural Science Foundation (2019GXNSFFA245008), National Natural Science Foundation of China (12073007), the Guangxi Natural Science Foundation (GKAD19245136; 2018GXNSFAA050001), and Scientific research project of Guangxi University for Nationalities (2018KJQD01), National Natural Science Foundation of China (11763001). MFG is supported by the National Science Foundation of China (grant 11873073). Zhi-Cheng He is supported by NSFC-11903031, NSFC 12192221, and USTC Research Funds of the Double First-Class Initiative YD 3440002001. Fu-Lai Guo is supported by National Natural Science Foundation of China (11873072).

References

Aird, J., Nandra, K., Laird, E. S., et al. 2010, *MNRAS*, 401, 2531
 Bentz, M. C., Denney, K. D., Grier, C. J., et al. 2013, *ApJ*, 767, 149
 Cardelli, J. A., Clayton, G. C., & Mathis, J. S. 1989, *ApJ*, 345, 245

Chen, Z.-F., Gu, Q.-S., & Chen, Y.-M. 2015, *ApJS*, 221, 32
 Chen, Z.-F., Huang, W.-R., Pang, T.-T., et al. 2018a, *ApJS*, 235, 11
 Chen, Z.-F., Pan, D.-S., Pang, T.-T., & Huang, Y. 2018b, *ApJS*, 234, 16
 Chen, Z.-F., Yi, S.-X., Pang, T.-T., et al. 2019, *ApJS*, 244, 36
 Condon, J. J., Cotton, W. D., Greisen, E. W., et al. 1998, *AJ*, 115, 1693
 Duan, X. & Guo, F. 2018, *ApJ*, 861, 106
 Elvis, M. 2000, *ApJ*, 545, 63
 Elvis, M. 2017, *ApJ*, 847, 56
 Fan, J.-H., Yang, J.-H., Pan, J., & Hua, T.-X. 2011, *Research in Astronomy and Astrophysics*, 11, 1413
 Ferland, G. J., Chatzikos, M., Guzmán, F., et al. 2017, *Rev. Mexicana Astron. Astrofis.*, 53, 385
 Ferland, G. J., Hu, C., Wang, J.-M., et al. 2009, *ApJL*, 707, L82
 Ferrarese, L. & Merritt, D. 2000, *ApJL*, 539, L9
 Gaskell, C. M. & Goosmann, R. W. 2013, *ApJ*, 769, 30
 Gaskell, C. M. & Goosmann, R. W. 2016, *ApSS*, 361, 67
 Gaspari, M., Ruszkowski, M., & Oh, S. P. 2013, *MNRAS*, 432, 3401
 Gaspari, M. & Sądowski, A. 2017, *ApJ*, 837, 149
 Gatti, M., Lamastra, A., Menci, N., Bongiorno, A., & Fiore, F. 2015, *A&Ap*, 576, A32
 Grier, C. J., Pancoast, A., Barth, A. J., et al. 2017, *ApJ*, 849, 146
 Gu, M., Chen, Z., & Cao, X. 2009, *MNRAS*, 397, 1705
 Guo, F., Duan, X., & Yuan, Y.-F. 2018, *MNRAS*, 473, 1332
 Hall, P. B., Brandt, W. N., Petitjean, P., et al. 2013, *MNRAS*, 434, 222
 Hamann, F., Simon, L., Rodríguez Hidalgo, P., & Capellupo, D. 2012, in *Astronomical Society of the Pacific Conference Series*, Vol. 460, *AGN Winds in Charleston*, ed. G. Chartas, F. Hamann, & K. M. Leighly, 47
 Häring, N. & Rix, H.-W. 2004, *ApJL*, 604, L89
 Heckman, T. M. & Best, P. N. 2014, *ARA&Ap*, 52, 589
 Hernquist, L. 1990, *ApJ*, 356, 359
 Hu, C., Wang, J.-M., Ho, L. C., et al. 2008, *ApJ*, 687, 78
 Kormendy, J. & Ho, L. C. 2013, *ARA&Ap*, 51, 511
 Li, Y. & Bryan, G. L. 2014, *ApJ*, 789, 153
 Madau, P. & Dickinson, M. 2014, *ARA&Ap*, 52, 415
 Menci, N., Gatti, M., Fiore, F., & Lamastra, A. 2014, *A&Ap*, 569, A37
 Mor, R. & Netzer, H. 2012, *MNRAS*, 420, 526
 Nenkova, M., Sirocky, M. M., Nikutta, R., Ivezić, Ž., & Elitzur, M. 2008, *ApJ*, 685, 160
 Nestor, D., Hamann, F., & Rodríguez Hidalgo, P. 2008, *MNRAS*, 386, 2055
 Netzer, H. 2015, *ARA&Ap*, 53, 365
 Pâris, I., Petitjean, P., Ross, N. P., et al. 2017, *A&Ap*, 597, A79
 Pei, Z.-Y., Fan, J.-H., Bastieri, D., Sawangwit, U., & Yang, J.-H. 2019, *Research in Astronomy and Astrophysics*, 19, 070
 Pei, Z.-Y., Fan, J.-H., Bastieri, D., et al. 2020, *Research in Astronomy and Astrophysics*, 20, 025
 Proga, D. 2007, *ApJ*, 661, 693
 Richards, G. T., Lacy, M., Storrie-Lombardi, L. J., et al. 2006, *ApJS*, 166, 470
 Schlafly, E. F. & Finkbeiner, D. P. 2011, *ApJ*, 737, 103

- Shen, S., Mo, H. J., White, S. D. M., et al. 2003, MNRAS, 343, 978
Shen, Y., Richards, G. T., Strauss, M. A., et al. 2011, ApJS, 194, 45
Shi, X.-H., Pan, X., Zhang, S.-H., et al. 2017, ApJL, 843, L14
Simões Lopes, R. D., Storchi-Bergmann, T., de Fátima Saraiva, M., & Martini, P. 2007, ApJ, 655, 718
Storchi-Bergmann, T. & Schnorr-Müller, A. 2019, Nature Astronomy, 3, 48
Treister, E., Schawinski, K., Urry, C. M., & Simmons, B. D. 2012, ApJL, 758, L39
Vestergaard, M. & Wilkes, B. J. 2001, ApJS, 134, 1
Weymann, R. J., Williams, R. E., Peterson, B. M., & Turnshek, D. A. 1979, ApJ, 234, 33
Wild, V., Kauffmann, G., White, S., et al. 2008, MNRAS, 388, 227
Zhang, N.-X., Brandt, W. N., Ahmed, N. S., et al. 2017, ApJ, 839, 101
Zhou, H., Shi, X., Yuan, W., et al. 2019, Nat, 573, 83